NANO LETTERS

LETTER

pubs.acs.org/NanoLett

Nanoconfinement of Spider Silk Fibrils Begets Superior Strength, Extensibility, and Toughness

Tristan Giesa,[†,‡] Melis Arslan,[†] Nicola M. Pugno,[§] and Markus J. Buehler*[,†]

[†]Laboratory for Atomistic and Molecular Mechanics, Department of Civil and Environmental Engineering, Massachusetts Institute of Technology, 77 Massachusetts Avenue, Room 1-235A&B, Cambridge, Massachusetts 02139, United States

[‡]Department of Mechanical Engineering, RWTH Aachen University, Templergraben 55, 52056 Aachen, Germany

[§]Laboratory of Bio-Inspired Nanomechanics "Giuseppe Maria Pugno", Department of Structural Engineering, Politecnico di Torino, Corso Duca degli Abruzzi 24, 10129, Torino, Italy

ABSTRACT: Silk is an exceptionally strong, extensible, and tough material made from simple protein building blocks. The molecular structure of dragline spider silk repeat units consists of semiamorphous and nanocrystalline β-sheet protein domains. Here we show by a series of computational experiments how the nanoscale properties of silk repeat units are scaled up to create macroscopic silk fibers with outstanding mechanical properties despite the presence of cavities, tears, and cracks. We demonstrate that the geometric confinement of silk fibrils to diameters of 50 $\pm$ 30 nm is critical to facilitate a powerful mechanism by which hundreds of thousands of protein domains synergistically resist deformation and failure to provide enhanced strength, extensibility, and toughness at the macroscale, closely matching experimentally measured mechanical properties. Through this mechanism silk fibers exploit the full potential of the nanoscale building blocks, regardless of the details of microscopic loading conditions and despite the presence of large defects. Experimental results confirm that silk fibers are composed of silk fibril bundles with diameters in the range of 20−150 nm, in agreement with our predicted length scale. Our study reveals a general mechanism to map nanoscale properties to the macroscale and provides a potent design strategy toward novel fiber and bulk nanomaterials through hierarchical structures.

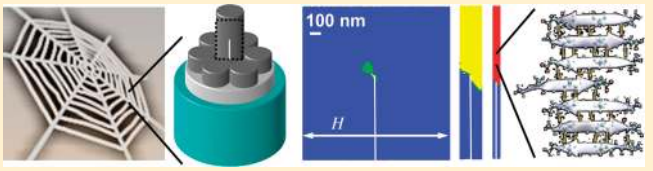

KEYWORDS: Spider silk, mechanical properties, deformation, geometric confinement, molecular simulation, coarse-grain model, materiomics

The great appeal of exploring spider silk, an ancient biological protein material (Figure 1a), lies in its intriguing mechanical properties that emerge in spite of the material's simple protein building blocks.[1−5] While there are many types of silk with different properties, we focus on the dragline silk of orb-weaving spiders that is known to be extremely strong, extensible, and tough.[6−9] Silk fibers typically feature an initial modulus up to 10 GPa,[8−10] a high extensibility exceeding 50−60% strain at failure,[8−11] and a tensile strength of 1−2 GPa,[8−10,12] which results in toughness values of several times that of Kevlar.[13] In addition to the relatively large ultimate strength of spider silk, comparable to that of steel, silk features a strength-to-density ratio that is up to ten times higher than that of steel because of the material's small density ($\approx$1.3 g/cm^3). As shown in Figure 1a, silk features a hierarchical structure, where the nanoscale geometry is characterized by a network of silk repeat units that each consist of a β-sheet nanocrystal embedded in semiamorphous protein domains. The sequence of silk repeat units (in one-letter amino acid codes, here as an example for MaSp1) is (GGAGQGGYGGLGSQGAGRGGLGGQGAG**AAAAAA**GG-AGQGGYGGLGSQGAGRGGLGGQG AG)$_N$ where the bolded 'A' identifies the region that forms β-sheet nanocrystals and the rest forms semiamorphous domains.

The mechanical behavior of silk fibers under tensile stretching is highly nonlinear. Beyond an initial high-stiffness regime, spider silk softens at the so-called 'yield point' where the stress−strain response gives way to a plateau, eventually leading to a stiffening regime prior to failure.[14] These mechanisms result in the characteristic softening−stiffening stress−strain response that is found for many different types of silk.[8−10] Previous investigations of silk have been focused at either the molecular[15−19] or the macroscopic scale.[20−22] Molecular-level studies elucidated the structure and role of β-sheet nanocrystals and semiamorphous protein domains during deformation, and the mechanical parameters for the behavior of a single repeat unit of silk were extracted.[17−19] At a much larger scale, experimental studies have shown that silk fibers contain many defects that act as stress concentrators, including cavities, surfaces, or tears[23−25] (further details see Methods Section). For example, Figure 1b shows images of crack-like cavities in *Nephila madagascariensis* dragline silk.[23] These defects feature sizes that reach several hundred nanometers and are crucial in the consideration of mechanical properties, as they serve as seeds for material failure through localized deformation (in fracture mechanics defects are known to lead to local stress concentrations).[26,27] Nevertheless, despite the presence of defects, silk fibers display remarkable mechanical properties.[28,29]

Received: September 7, 2011
Revised: September 27, 2011
Published: October 04, 2011

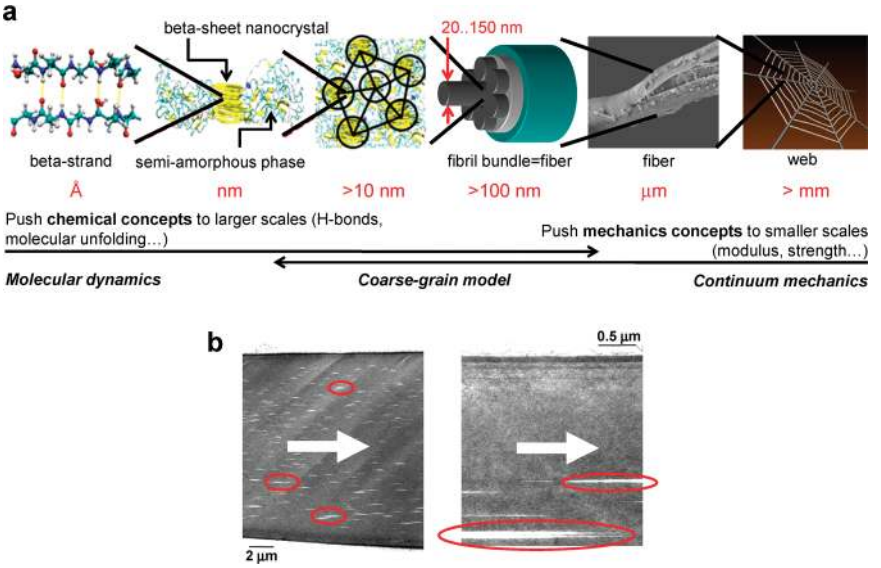

Figure 1. Hierarchical levels in spider silk including detailed views of the microscale structure and flaws in silk fibers. (a) Schematic structure of spider silk from nanoscale to macroscale. The image second from right reprinted from ref 25, copyright 2002, with permission from Elsevier, and the image third from right shows the silk fiber bundle model where silk fibrils are found experimentally to be confined to diameters in the range from 20 to 150 nm.[11,22−24,30] A coarse-grain model is used here as a tool to push chemical concepts to larger scales and to push mechanical concepts to smaller scales, representing the network of silk repeat units. (b) Microscopic images of *Nephila madagascariensis* dragline silk fibers showing the skin−core structure as well as flaws and cavities in the material. The white arrows point in the axial fiber direction, and the red ellipses highlight some of the defects found in the structure. Pictures reprinted from ref 23, copyright 1998, with permission from John Wiley & Sons, Inc.

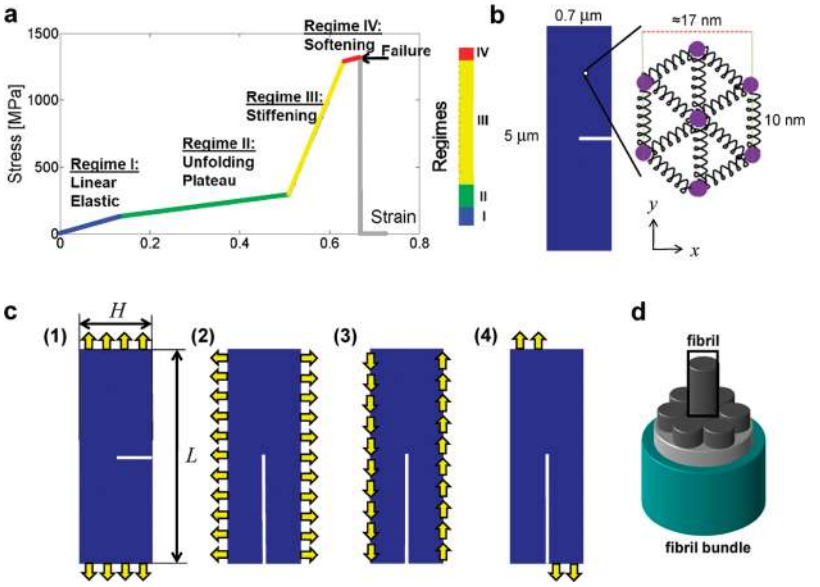

Figure 2. Model of the silk fibril, geometry, and loading conditions considered. (a) Stress−strain behavior for a defect-free silk fiber, noting the key transition points between the four regimes marked by molecular events at the molecular scale.[17−19] The transition from regime I to II marks the onset of unfolding of the semiamorphous phase of silk; the transition from regime II to III marks the onset of stretching of the β-sheet nanocrystal phase. In regime IV, β-sheet nanocrystals fail via a stick−slip mechanism, eventually leading to failure. (b) Triangulated network model with similar length scales to that of the molecular structure seen in Figure 1a, where the spacing between particles corresponds to the distance between β-sheet nanocrystals; used here to model a larger scale silk fibril with dimensions of several micrometers. (c) Loading conditions used in the simulations, implementing tensile [mode I, (1) and (2)] and shear [mode II, (3) and (4)] loading with varied aspect ratio. In the simulations the fibril length L is kept constant, while the fibril width H is varied. The crack is sharp and runs through 50% of the respective dimension. (d) 'Skin−core model' of silk fibers consisting of bundles of fibrils (schematic; number of fibrils in a bundle is larger than shown here).

The mechanism by which the nanoscale properties of silk, originating from the interplay of β-sheet nanocrystals and semi-amorphous protein domains, are scaled up to the macroscale remains unknown. Addressing this issue requires an analysis that covers multiple scales from nano to macro. Full-atomistic modeling[17−19] cannot reach the micrometer scales associated

dx.doi.org/10.1021/nl203108t |*Nano Lett.* 2011, 11, 5038–5046

with the characteristic dimensions of silk fibers and defects.[23,28,29] Continuum models, on the other hand, are size-scale independent and lack the capacity to describe the material behavior from the bottom-up, and parameters are typically fitted to experimental results. To overcome these limitations here, we use a coarse-grain mesoscale model as a tool to bridge the gap in scales.[30] We represent the network of silk repeat units in silk fibers in a triangulated network with a particle-to-particle distance of 10 nm. By using large-scale computing, we reach length scales of several micrometers while retaining information about the underlying molecular mechanisms (Figure 2a,b). In the development of the coarse-grain model the behavior of a single repeat unit of silk[19] is used to identify the parameters for particle−particle interactions at the mesoscale (see Methods Section).

By establishing a molecular basis for the formulation of the coarse-grain model, we incorporate a mechanistic understanding of the origin of the different deformation regimes based on the interplay of β-sheet nanocrystals and semiamorphous domains. Figure 2a shows the stress−strain behavior of a defect-free silk fiber and indicates four key deformation regimes. The plot also shows the associated color code used for the field plots depicted in the subsequent figures. Regime I is characterized by a linear-elastic response dominated by homogeneous stretching before protein unfolding begins. The transition from regime I to II is marked by the beginning of the rupture of H-bonds in 3_1-protein helices that make up the semiamorphous domains, and the unraveling of these proteins continues until all hidden length is exhausted. Thereby, regime II is the key to the extensibility of silk. Regime III reflects the stiffening behavior that sets in after the exhaustion of unfolding events and the alignment of polypeptide chains. This facilitates the deformation of β-sheet nanocrystals that leads to a significant stiffening of the material in regime III. Regime IV involves a brief softening behavior as β-sheet nanocrystals fail under stick−slip deformation leading to the breakdown of β-sheet nanocrystal cross-links and eventual material failure. The mechanical stability of β-sheet nanocrystals is the key to the ultimate strength molecular-level silk since they are the last molecular elements that break.[19] The importance of the β-sheet nanocrystal stability and their dependence on the geometry has been discussed in earlier works, emphasizing the role of their nanoconfinement to dimensions on the order of 2−4 nm.[16,18]

In order to explore the natural loading conditions of silk fibers with consideration of different types of defects, a set of different boundary conditions is considered (Figure 2c). Loading conditions (1) and (2) are both tensile and resemble mode I loading. Typically, silk fibers bear axial tension, with the most 'classical' condition being (1). Longer fibers can also be exposed to shear loading due to slip between adjacent fibers, represented by loading conditions (3) and (4) that resemble mode II in shear and tear loading. We consider a stress concentrator as a model for structural inhomogeneities (Figure 2b)[23,26,27] and implement a sharp crack that runs along the midline of a microscale slab with dimensions $0.70 \times 5\,\mu m^2$, representing a fiber with $H \times L$, where the width of the fibril is H and the length of the fibril is L. The dimensions resemble the typical size found in natural silk fibers with a diameter H on the order of micrometers and a length that is several times larger than the width ($L \gg H$). Although we expect most cracks to be transverse to the fiber axis, visual analyses of experimental results motivate the evaluation of the influence of cracks oriented in the axial direction.

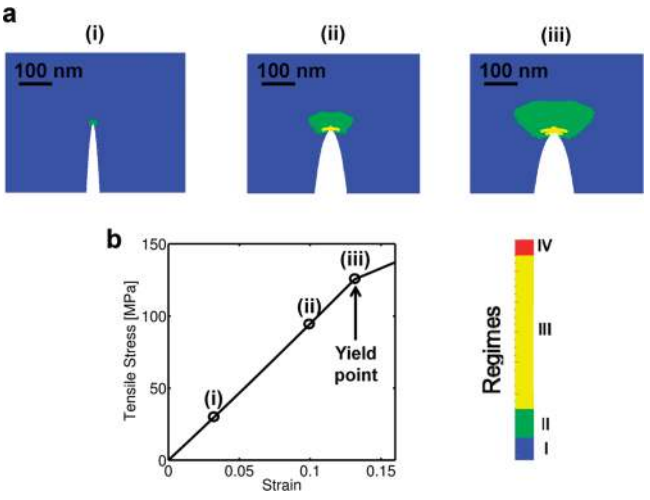

Figure 3. Macroscale deformation behavior and evolution of molecular unfolding events close to the crack tip as the applied strain is increased under tensile loading. (a) Snapshots of the deformation field as the applied strain is increased, corresponding to the points shown in the stress−strain plot shown in (b) (color code for the different deformation regimes shown below panel (iii), corresponding to the regimes shown in Figure 2a): (i) Deformation field at ≈3% applied strain when a small region (confined to ≈10 nm length) has entered the unfolding regime; (ii) deformation field at ≈10% applied strain; and (iii) deformation field at ≈13% applied strain when macroscale softening occurs as shown in (b), marked as the 'yield point'. At ≈13% applied strain, the region that has undergone molecular unfolding (regime II) is confined to a length-scale of ≈120 nm, and the region in which β-sheet nanocrystals are being stretched (regime III) extends to ≈23 nm. (b) Macroscale stress−strain curve with locations indicated that relate to the snapshots shown in (a). Upon softening, the material fails shortly thereafter at 15% strain when the macroscale stress drops to zero. This maximum strain is significantly smaller than observed in experiment, where strains of up to 60% are reached (e.g., ref 8) and where the stress−strain behavior shows a stiffening regime before breaking.

Results. We plot the deformation field at the edge of a sharp crack as the applied loading is increased (Figure 3). The percolation of the molecular deformation mechanisms in the fiber domain is shown in Figure 3a, combined with the corresponding stress−strain response depicted in Figure 3b. Different colors in the snapshots reflect the different molecular-scale mechanisms associated with the regimes described above (blue = regime I, green = regime II, yellow = regime III, and red = regime IV; see Figure 2a). The snapshots in Figure 3a start from the applied strain, where the first particles at the edge of the crack reach the strain associated with transitioning from regime I to II, at 3% applied strain and at which unfolding of the bonds in the semiamorphous phase begins. A linear deformation regime prior to the yielding point (13% strain) is observed (Figure 3b), and the fiber fails at an applied strain of less than 15%. This is much *smaller* than experimentally observed failure strains of silk fibers and much *before* the onset of the stiffening regime that follows the yield point as seen in numerous experiments.[8,11,12,28] An analysis of the data shown in Figure 3a reveals that as the applied strain is increased, the number of bonds that enter regime II (molecular unfolding of the semiamorphous phase) increases significantly but approaches a finite value at the failure point. The third snapshot Figure 3a(iii) refers to the macroscale strain level at which the overall material response begins to soften (Figure 3b), marking the yield point. The extension of the region

dx.doi.org/10.1021/nl203108t |*Nano Lett.* 2011, 11, 5038–5046

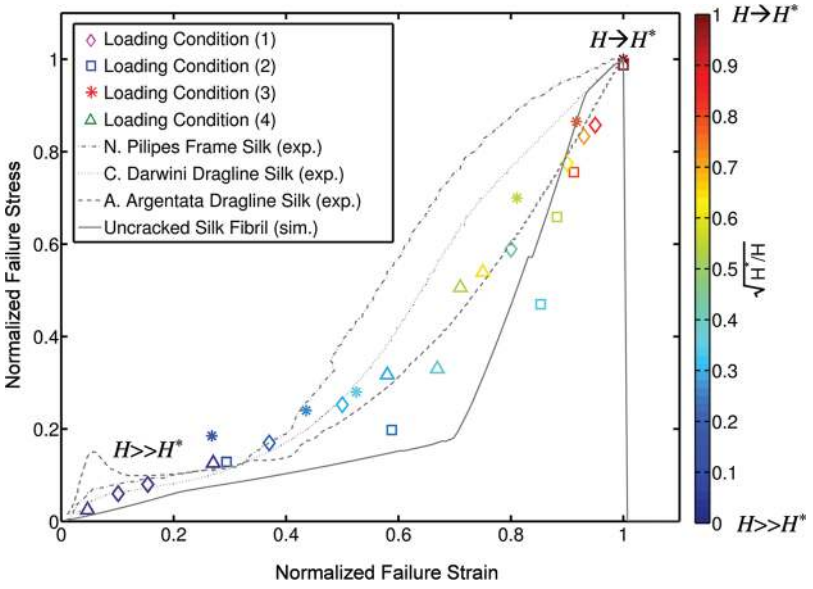

Figure 4. Dependence of the failure strain and failure stress on the fibril size H as well as a direct comparison with experimental results and the mechanical behavior of a defect-free silk fiber. For decreasing fibril sizes, the perfect material behavior (i.e., ≈1400 MPa failure stress and 68% failure strain) is approached and reached at $H = H^*$. For loading conditions (2) and (3), we find $H^* \approx 77$ nm, and for loading conditions (1) and (4), $H^* \approx 22$ nm (Figure 2c). The simulation of a defect-free, uncracked silk fiber is shown for comparison as well as experimental data (*Nephila pilipes* frame silk fails at ≈1050 MPa and 40% strain,[28] *Caerostris darwini* dragline silk at ≈1700 MPa and 80% strain,[8] and *Argiope argentata* dragline silk fails at ≈1800 MPa and 25% strain).[8] The results show that the high strength and extensibility observed in experimental studies can only be reached by nanoconfinement of fibrils close to $H^* \approx 50 \pm 30$ nm.

that has entered regime II at the yield point can be quantified by an effective yield radius that is estimated to be $(A_{\text{unfold}}/\pi)^{1/2} \approx$ 120 nm.

This implies that under the presence of stress concentrators there exists a relatively small region of the material that has entered regime II, extending over only ≈10 silk repeat units in each direction. Further inspection of the deformation field at the yield point shown in Figure 3a(iii) reveals an even smaller region with an effective radius of ≈23 nm, where the molecular bonds have already entered regime III during which the cross-linking β-sheet nanocrystals are deformed. A very similar behavior is seen in all other loading cases including shear loading, showing that this is a general result regardless of the specific loading conditions. The observation of significant localization of molecular unfolding of silk repeat units that enter regimes II and III suggests the existence of a characteristic length scale that determines the failure properties of silk at the fiber scale. Indeed, in the silk fiber considered here only a very small fraction of less than 1% of the entire material present in the fiber actually contributes to its larger-scale mechanical properties, while most protein domains (more than 99%) do not contribute.

We now explore the mechanical behavior of the fiber as the diameter is reduced toward values that match the critical length scales identified above. This is achieved by carrying out a series of computational experiments during which we consider samples with decreasing fiber width H while all other parameters are kept constant, including the length of the fiber and the dimensionless length of the crack which runs through half the fiber. We monitor the stress−strain response of each sample and for all four loading conditions. We find that as the width H is reduced, the fiber's mechanical properties undergo a drastic change and reach successively higher failure stresses and strains (Figure 4). It is seen that the fibers fail at the strength and extensibility close to the properties of a perfect defect-free fiber, once H approaches values of around $H^* \approx 50 \pm 30$ nm. Notably, the existence of the very large defect included in all cases considered here does not compromise the mechanical performance. Most importantly, the stress−strain curves of stretching fibers with small widths agree well with a range of experimental data taken at the fiber scale,[8,11,12,28,31] as shown directly in Figure 4.

To understand the origin of this behavior, we compute the area percent of the material that has entered regime IV (at which β-sheet nanocrystals fail) and plot this quantity for varied sizes H for loading conditions (1−4) (Figure 5a). The analysis shows that there exists a sudden transition at a critical length-scale $H = H^*$. When $H \gg H^*$, only a vanishingly small fraction of the material contributes to resisting failure. When $H \rightarrow H^*$, virtually all material in the fiber contributes to its mechanical properties. We find the critical size H^* to be $H^* \approx 22$ nm for loading conditions (1) and (4) and $H^* \approx 77$ nm for loading conditions (2) and (3). We perform a similar analysis for the area percent of the material that has entered regime III and find a transition at $H^{**} \approx 155$ nm for loading condition (1) and (4) and $H^{**} \approx$ 510 nm for loading conditions (2) and (3). At the length scale H^{**}, however, the fiber does not display the characteristic stiffening regime yet and, as a result, shows a significantly smaller failure stress and toughness compared with the defect-free case (Figure 4). As can be clearly seen from the data presented in Figure 4, fiber widths of $H^* \approx 50 \pm 30$ nm are crucial to exploit the full potential of the material and to reach all four regimes of deformation at the macroscale, including the final stiffening regime, regardless of the details of the loading condition and in spite of the presence of very large defects.

Recent experimental studies[8] suggest that dragline silk of larger spiders attains toughness moduli that range from ≈100 up to 350 MJ/m^3 (across various species) with the largest values exceeding ≈500 MJ/m^3 . The experimental toughness moduli values agree remarkably well with the values calculated from our

dx.doi.org/10.1021/nl203108t |*Nano Lett.* 2011, 11, 5038–5046

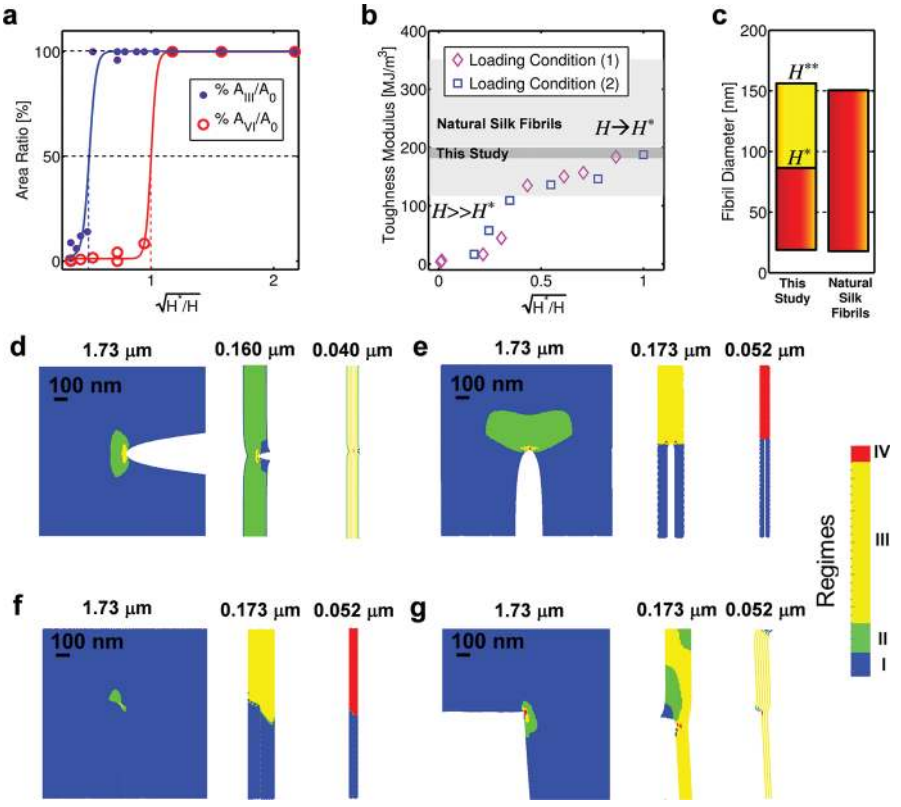

Figure 5. Geometric analysis of failure mechanisms. (a) Percentage of the slab area that has reached regimes III and IV [the maximum attainable fraction A_0 equals 100% of the slab for loading condition (1), 50% of the slab for loading conditions (2) and (3), and 75% of the slab for loading condition (4)]. The results for regime IV confirm that below the critical length $H^* \approx 77$ nm [loading conditions (2) and (3)] or $H^* \approx 22$ nm [loading conditions (1) and (4)] the entire slab contributes to the strength, marking a massive increase at small H compared with the cases for large H. (b) Toughness modulus for tensile loading conditions (1) and (2). By geometric confinement, the theoretical toughness modulus (190−200 MJ/m^3) is approached which is in good agreement with experimental toughness moduli represented in the light-gray shaded area (110−350 MJ/m^3). (c) Comparison of experimentally determined diameters H in natural silk fibrils to the simulation results. Nanoconfinement to $H^* \approx 50 \pm 30$ nm yields a homogeneous deformation state, whereas a confinement to $H^{**} \approx 155$ nm ensures complete unfolding of the semiamorphous phase for the 'natural' loading condition (1). (d) Series of snapshots taken at the failure point of each fibril, for varied slab widths, under tensile loading [mode I, (1)]. (e) Series of snapshots taken at the failure point, for varied slab widths, under tensile loading with different aspect ratio [mode I, (2)]. A similar behavior as in loading case (1) is observed here, where the deformation field becomes increasingly homogeneous as the size is reduced. Failure also occurs at the failure stress and strain corresponding to a defect-free slab. (f) Series of snapshots taken at the failure point, for varied slab widths, under shear loading [mode II, (3)]. A similar behavior as found in mode I, loading condition (2), is observed. (g) Series of snapshots taken at the failure point, for varied slab widths, under shear loading [mode II, (4)]. A similar behavior as found in mode I, loading condition (1), is observed. Images shown in (d−g) show only a small fraction of the entire fiber close to the crack tip.

model that are estimated to be 190−200 MJ/m^3 (Figure 5b). Our results show that these superior toughness moduli are *only* accessible provided that the fibers are confined to dimensions below the critical length scale H^*, where the extensibility due to regime II (unfolding plateau) is combined with the high tensile strength defined by the breaking of β-sheet nanocrystals in regime IV. Indeed, for larger fibers with $H > H^*$, the toughness moduli reach only a small fraction of those seen in experimental work. A fiber with width 1.73 μm, for example, reaches a toughness modulus of only 10−20 MJ/m^3, which is in stark contrast to experimental findings. This provides evidence for the claim that fibrils in natural silk fibers are in a homogeneous deformation state at failure, which is quantitatively supported by the experimentally determined geometries and fiber properties (Figure 4).

Further insight into the link between the molecular-level mechanisms and the failure behavior under varied fiber widths is gained by investigating the deformation fields. Figure 5d−g shows the deformation fields for varied sample widths H for tension (loading conditions (1) and (2), Figure 5d,e) and shear (loading conditions (3) and (4), Figure 5f,g). While deformation is highly localized to the crack tip region in the largest system considered (H = 1.73 μm) and in agreement with the results shown in Figure 3 and Figure 5a, deformation becomes more and more delocalized as the width approaches smaller dimensions below 150−550 nm (Figure 5d−g). For slab sizes smaller than $H^* \approx 50 \pm 30$ nm, deformation is completely homogeneous, and the entire sample reaches the maximum attainable stress before failure. This is a significant observation that implies that molecular unfolding of the semiamorphous phase (regime II) and the stretching and breaking of β-sheet nanocrystals (regimes III−IV) occurs throughout the *entire* sample, such that the *entire* material ahead of the defect contributes equally to resisting mechanical failure, providing a concerted action to enhance the strength and extensibility. For example, the concerted rupture of β-sheet nanocrystals extends over an area of 77 nm × 2.5 μm.

dx.doi.org/10.1021/nl203108t |*Nano Lett.* 2011, 11, 5038–5046

Table 1. Summary of Key Structures and Associated Mechanisms of Upscaling from the Atomistic to Larger Scales[a]

structural detail	scale/level	mechanism
β-strand	Å/nm	critical β-strand length for heightened stability of H-bond clusters; cooperativity of H-bonds maximized at a critical scale of 3−4 H-bonds[36]
β-sheet nanocrystals	nm	critical β-sheet crystal size between 2 and 4 nm allows for robust and shear-dominated deformation, enabled by cooperative action of clusters of H-bonds[16,18,28]
fibrils	sub-μm	homogeneous deformation state reached if fibril dimension confined to $H^* \approx 50 \pm 30$ nm width; enables concerted contribution of massive numbers of β-sheet nanocrystals across entire fibril length of several micrometers (see Figure 5d−g in this study for direct visualization)
fibers	μm	bundling of several fibrils into fibers where each fibril is in homogeneous deformation state; akin to concept of structure splitting mechanism[38] where bundles of fibrils are assembled into fibers to enhance the overall mechanical properties
spider web	cm	characteristic softening−stiffening nonlinear material behavior of spider silk combined with the discrete structure of the spider web leads to localized failure of webs[39]

[a] See also Figure 1a for an overview of structural levels in spider silk.

This shows that, provided $H \rightarrow H^*$, hundreds of thousands of repeat units (and thus, protein domains) interact synergistically in defining the mechanical properties of the fibril through a completely percolated network of unfolding protein domains.

Both loading conditions, tensile (2) and shear (3), display the same mechanisms and an equal critical slab width of H^*. A similar behavior is observed for loading conditions (1) and (4), where the critical slab width of H^* is around three times smaller. The origin of the difference of H^* between the loading conditions can be explained by linear-elastic fracture mechanics. We compare loading conditions (1) and (2) (both mode I) and determine the ratio of the critical slab size H^* associated with the ideal strength of the defect-free material and find $H_1^*/H_2^* = 1/\pi$ (details see Methods Section). This ratio is in good agreement with our simulation results and implies that despite the highly nonlinear behavior, the mechanisms leading to the homogeneous deformation state can be qualitatively explained by linear-elastic fracture theory. On the other hand, the result confirms that the homogeneous deformation state is boundary condition dependent. Specifically, the value of H^* depends on the specific loading conditions, which is accounted for in our study by explicitly considering a set of cases which results in identifying a range of H^* rather than a single value.

Discussion. The homogeneous deformation state of silk fibers presents upscaling mechanisms that help us to quantitatively explain the role of hierarchical structures seen in silk fibers, including the skin−core model where bundles of smaller fibrils make up larger fibers (Figures 1a and 2d).[26,27,32] Indeed, experimental work showed that the diameters of silk fibrils are on the order of 20−150 nm,[13,26−28,32] as shown in Figure 5c in agreement to the length-scale ranges of H^* and H^{**} identified in our study. Silk fibrils, by means of confinement to the critical length-scale below H^*, each reach a homogeneous deformation state. Since silk fibers are relatively small bundles of only tens to hundreds of silk fibrils, they behave similarly as individual silk fibrils and thereby enable silk fibers to maintain high strength and extensibility. Under the presence of flaws *smaller* than considered in this study (consistently 50% of width H or length L, respectively), individual fibrils can reach the homogeneous deformation state even at a *larger* critical size H^* (see Methods Section). An important insight derived from this finding is that molecular unfolding, β-sheet crystal rupture and other failure mechanisms span the entire structural scale of silk fibrils and up to several micrometers in length, given that the width of the fibrils is confined to the nanoscale. The extreme confinement of the fibril in one dimension (width) facilitates an extreme spreading of cooperative molecular unfolding in the other direction (length), where the length can be hundreds of times larger than the width. This also explains why the predictions from molecular simulations[17−19] of defect-free silk repeat units agreed well with experimental testing of macroscopic silk fibers. This concept of nanoconfinement makes molecular-scale properties directly visible at the macroscale and provides a powerful design strategy by which tuning the nanoscale structure and properties can directly affect macroscale material properties at its full potential.

The nanoscale structure of spider silk is characterized by weak interactions, such as H-bonds. The hierarchical arrangement of building blocks (Figure 1a) enhances its material properties so that the larger-scale properties provide a high level of functionality through the synergistic interaction of mechanisms at multiple scales (Table 1). The emergence of increased structural stability driven by geometric confinement is a recurring pattern that also exists at other scales in the hierarchical makeup of silk. For example, as shown earlier,[16] the stability of β-sheet nanocrystals is greatly enhanced when confined to sizes of 2−4 nm, a finding that also agrees with recent molecular modeling studies[18] and experimental results[28] that suggested a similar length scale. Our results complement these earlier findings by demonstrating that the stability of β-sheet nanocrystals is made visible at micrometer-length scales through the use of bundles of fibrils with $H^* \approx 50 \pm 30$ nm width. An overview of various mechanisms at different hierarchical levels of silk fibers is shown in Table 1.

Size effects associated with the fracture of materials has been postulated already by Griffith in the early 20th century.[33−35] The availability of advanced computational and experimental methods makes it now possible to quantitatively explore the fracture mechanics of complex hierarchical materials, such as spider silk, from a bottom-up perspective and to identify critical length scales that define their mechanical properties at various levels[16,28,36−39] and link these with molecular deformation mechanisms. Griffith stated that the ideal molecular level strength is reached as their characteristic size reduces to that of the molecules. Our work shows that in silk, the ideal strength of the defect-free material is reached at scales of around $H^* \approx 50 \pm 30$ nm, which encompasses hundreds of thousands of protein molecules per fibril that

dx.doi.org/10.1021/nl203108t |*Nano Lett.* 2011, 11, 5038–5046

interact synergistically. This marks a departure from Griffith's hypothesis that the ideal strength of a material can only be reached at the scale of atomic spacing (a few Å) and is explained by the hierarchical structure of silk (Table 1). We note that the hierarchical structure of silk implies a departure from the linear-elastic stress−strain law assumed in classical fracture mechanics, explaining the disagreement with the classical result. Indeed, hierarchical structures in other biological materials have also been shown to enhance their performance at larger scales through mechanisms of flaw-tolerance similar as what is seen here (see, for example, refs 34 and 40−44). In particular the concept of bundling smaller fibrils into fibers resembles the structure splitting mechanism[45] proposed for bulk materials, such as bone and nacre. In bone, nacre and many other biomaterials, larger-scale mechanisms, such as crack bridging, microcracking, and others, contribute significantly to the overall toughness of the material. It remains an open question whether such mechanisms play an important role in silk. An interesting avenue for future studies could be an analysis of the effect of different nanoscale architectures of the protein network on the macroscale behavior.

Conclusion. Coupling the behavior of nanoscale silk repeat units with the mechanical response of macroscale silk fibers, the superior performance of silk does not need to rely on strong bonding at the nanoscale. Rather, it relies on the integration of material and structure across all scales, which enables a mechanism that utilizes weak bonds and simple material building blocks at its full potential. This paradigm, developed here based on silk as a model biological material but valid for many other natural and synthetic materials, explains the fundamental issue of how achieving functionality in biological materials extends beyond conventional concepts used in engineered materials where strong bonding serves as a primary route to achieve superior mechanical properties.

Methods. *Coarse-Grain Model.* As a bridge between the atomistic and the continuum scale, we use a mesoscale coarse-grain model. We implement a simple planar (plane strain) quasi-two-dimensional particle model where the mesh is a triangulated network with a particle−particle distance of r_0 = 10 nm and a periodic thickness of t = 1 nm (see Figure 2b), close to structural data obtained from experimental work by Du et al.[28] To implement a stress concentrator as a model for inhomogeneities, such as cavities,[23,26,27] we consider a set of different loading conditions as shown in Figure 2b, where the width of the slab is varied for different cases studied under constant length of 5 μm. We deform the slab under both quasi-static tensile (mode I) and shear (mode II) loading with varied aspect ratio to assess the mechanisms.

Model Formulation and Parameters. A triangulated network model is used to match the nonlinear behavior seen in molecular simulation[17−19] and marked by the four distinct regimes I−IV: linear-elastic response, unfolding plateau stiffening behavior, and final softening (detailed molecular mechanisms discussed in the main text). The force−extension behavior for each coarse-grained bond is given by:

$$F_b(\lambda_b) = \begin{cases} k_1 r_0(\lambda_b - 1), & 1 < \lambda_b < \lambda_{b1} \\ k_1 r_0(\lambda_{b1} - 1) + k_{1-2} r_0(\lambda_b - \lambda_{b1}), & \lambda_{b1} < \lambda_b < \lambda_{b2} \\ k_1 r_0(\lambda_{b1} - 1) + k_{1-2} r_0(\lambda_{b2} - \lambda_{b1}) + k_{2-3} r_0(\lambda_b - \lambda_{b2}), & \lambda_{b2} < \lambda_b < \lambda_{b3} \\ k_1 r_0(\lambda_{b1} - 1) + k_{1-2} r_0(\lambda_{b2} - \lambda_{b1}) + k_{2-3} r_0(\lambda_{b3} - \lambda_{b2}) + k_{3-4} r_0(\lambda_b - \lambda_{b3}), & \lambda_{b3} < \lambda_b < \lambda_{b4} \\ 0, & \lambda_b > \lambda_{b4} \end{cases} \quad (1)$$

where λ_{b1}, λ_{b2}, λ_{b3}, and λ_{b4} are the transition stretches for each bond. In order to link the constituent transition bond stretches to the macroscopic transition stretches, we fit the initial elastic modulus and transition points using kinematic and constitutive relationships against atomistic data.[46] These transition strains are λ_{b1} = 1.10, λ_{b2} = 1.35, λ_{b3} = 1.45, and λ_{b4} = 1.50. Similarly, we fit the initial tensile modulus and determine the initial bond stiffness k_1 accordingly using an expression for the elastic modulus for linear-elastic isotropic triangulated networks,[46] resulting in $k_1 = \sqrt{3}E_0 t$ = 0.50 N/m, where the initial modulus is E_0 = 850 MPa. The bond stiffnesses in different regimes are similarly fit using the ratios of the stiffness changes as identified from molecular modeling resulting in k_{1-2} = 0.20 N/m, k_{2-3} = 3.75 N/m, and k_{3-4} = 0.30 N/m. The stress−strain behavior of a defect free silk fiber is depicted in Figure 2a.

The transition to a homogeneous deformation state (regime IV) of the slab occurs at a critical slab size $H = H^*$ and the transition to a completely unfolded state (regime III) at $H = H^{**}$. This transition occurs when 50% of the slab area contribute to the strength of the slab is in regime IV or regime III, respectively. The fits are sigmoidal functions in the form $A(H^*/H) = x_1 + (x_2 - x_1)/\{x_3 + x_4 \exp[-x_5(H^*/H - x_6)]\}$. For A_3, the best fit is x_1 = 0.01, x_2 = 0.29, x_3 = 0.60, x_4 = 0.70, x_5 = 36.6, and x_6 = 0.32, and for A_4, we find x_1 = 0.50, x_2 = 0.006, x_3 = 1.0, x_4 = 1.0, x_5 = −44.5, and x_6 = 0.83.

Mechanical Loading. We employ an energy minimization approach where for the tensile loading conditions [mode I, loading conditions (1) and (2)], 0.3% strain increments in the x-direction are applied as edge displacement followed by an energy minimization carried out using a conjugate gradient algorithm. A maximum of about 70% strain is applied to the structure until fracture of the entire system occurs. As for the shear loading conditions [mode II, loading conditions (3) and (4)], 0.1% shear strain in the $y-x$-direction is applied as edge displacement followed by an energy minimization carried out using the same algorithm. The shear strain is increased until fracture occurs. The stress fields are calculated based on the virial stress.[47] The model is not intended to reflect the specific boundary conditions present in silk (which are hard to know a priori) but is designed to assess fundamental size effects in this material, which we believe is best done in a sufficiently simple model system. The mode I loading case (2) has limited physical motivation but is of interest from a fracture mechanics point of view and adds an important aspect for studies of other systems. This approach has been used successfully in earlier studies[48] and provides fundamental insight into the mechanisms rather than making predictions about specific types of silk.

Defects in Natural Silk Fibers. While experimental analyses have clearly shown defects in silk fibers, they do not provide clear evidence about the exact geometry of the defects. Imaging techniques reveal either ordered structures[27,28,49] or imperfections.[23,24] Failure mode analyses of *Attacus atlas* and *Bombyx mori* cocoon silk showed that under tensile loading silk fibers fail by microfibril-pullout, whereas *Argiope trifasciata* spider silk displayed

dx.doi.org/10.1021/nl203108t |*Nano Lett.* 2011, 11, 5038–5046

fibrillar structures. Interfacial voids and decohesions found in the fibers could not be linked to failure mechanisms.[25] Although many of the macroscopic defects seem to have a penny-like shape in the fiber direction and an almost circular cross-sectional shape, the consideration of a sharp crack as a limiting case of fracture mechanical relevance appears reasonable. Without changing the nature of the results, computational modeling allows the straightforward study of arbitrary defect configurations that would cause an experimental challenge.

Implementation of Simulations. All simulations are carried out using the massively parallelized LAMMPS code.[50] The study reported here is an exemplification of the use of the multiscale modeling paradigm applied to realistically predict the strength, extensibility, and toughness of materials from the molecular scale upward (Figure 1a). It is noted that the boundary conditions of real fibrils may be different but hard to know in advance. Rather than making assumptions about one specific loading conditions, we consider several likely ones through the application of displacement loading to resemble modes I and II in four loading scenarios (Figure 2c). From a fracture mechanics point of view,[33,34,51] the setup used here, with only one length-scale H in the system (and the perpendicular dimension $\gg H$ with a long crack that runs half way through the width or length), provides a convenient and direct way to assess size effects.

Fracture Mechanics Analysis. The stress intensity factor for loading condition (1) with $L/H > 1$ is given by[51]

$$K_{IC,1} = \sigma_C\sqrt{\pi a}F\left(\frac{a}{H}\right) \cong \sigma_C\sqrt{\pi\frac{H}{2}} \quad (2)$$

and for loading condition (2) with $H < 4a/3$:

$$K_{IC,2} = \sigma_C\sqrt{\pi a}F_{1s}(s) \cong \sigma_C\sqrt{\frac{H}{2}} \quad (3)$$

where $L = 5\ \mu$m is the slab length, a the crack size, and σ_C the applied stress at failure (for definition of variables in equations above see [51]). The homogeneous deformation state can be assumed to be associated with the stress reaching its theoretical value of the defect-free bulk material σ_{th}.[32] Hence the transition occurs when $\sigma_C = \sigma_{th}$ (see eqs 2 and 3, where K_{IC} is the critical stress intensity factor, a material constant that describes the material fracture toughness). The comparison of the critical slab lengths yields:

$$\frac{H_1{}^*}{H_2{}^*} = \frac{2{K_{IC}}^2}{\sigma_{th}^2}\frac{\sigma_{th}^2}{2{K_{IC}}^2\pi} = \frac{1}{\pi} \approx 0.318 \quad (4)$$

which is in close agreement with our simulation results, where we find that $H_1^* \approx 22$ nm and $H_2^* \approx 77$ nm, leading to $(H_1^*/H_2^*)_{sim} \approx 0.286$. This suggests that linear-elastic fracture mechanics qualitatively describes the results. Further calculations are not feasible due to the lack of experimental values for the fracture toughness. *Higher* values of H^* are reached when the crack size is *smaller* than the 50% considered in this study, as can be seen from linear-elastic fracture mechanics (eq 2). From the point of view of fracture mechanics, the two-dimensional plane strain model of the fibril with a periodic crack and a three-dimensional cylinder with a circumferential crack display equal behavior.[51] Hence, our analysis with a two-dimensional planar particle model appropriately reflects the conditions found in real silk fibers.

Fibril and fibril bundle mechanical properties. Using a coarse-grained bead−spring model, parametrized to fit the stress−strain curves shown in Figure 4, we confirmed that bundles of hundreds of fibrils with widths of 50 ± 30 nm arranged into a silk fiber behave similarly as individual silk fibers (details not shown). Bundling 20−30 fibrils in the cross-sectional direction results in a fiber of ≈1 μm diameter which maintains the mechanical properties of individual fibrils and reaches the scales of naturally found silk fibers.

AUTHOR INFORMATION

Corresponding Author

*E-mail: mbuehler@mit.edu.

Author Contributions

T.G., M.A., and M.J.B. conceived and designed the model, computational experiments, and associated analysis. T.G. and M.A. set up, carried out, and processed the computational experiments. N.P. and T.G. contributed the fracture mechanics analysis. T.G., M.A., N.P., and M.J.B. analyzed the data and wrote the paper.

Notes

The authors declare that no competing interests exist.

ACKNOWLEDGMENT

N.M.P. is supported by the METREGEN grant (2009-2012): "Metrology on a cellular and macromolecular scale for regenerative medicine" All simulations have been carried out at MIT's Laboratory for Atomistic and Molecular Mechanics. Support from ARO-MURI (award no. W991NF-09-1-0541), National Science Foundation, ONR-PECASE (award no. N000141010562) and the German National Academic Foundation (Studienstiftung des deutschen Volkes) is acknowledged. We acknowledge helpful discussions on silk materials science with David Kaplan (Tufts University) and Joyce Wong (Boston University).

REFERENCES

(1) Kaplan, D. L. *Silk Polymers: Materials Science and Biotechnology*; American Chemical Society: Washington, DC, 1994; p 370.

(2) Omenetto, F. G.; Kaplan, D. L. *Science* **2010**, *329* (5991), 528–531.

(3) Vollrath, F. *Nature* **2010**, *466* (7304), 319–319.

(4) Rammensee, S.; Slotta, U.; Scheibel, T.; Bausch, A. R. *Proc. Natl. Acad. Sci. U.S.A.* **2008**, *105* (18), 6590–6595.

(5) Gosline, J. M.; Guerette, P. A.; Ortlepp, C. S.; Savage, K. N. *J. Exp. Biol.* **1999**, *202* (23), 3295–3303.

(6) Lewis, R. V. *Chem. Rev.* **2006**, *106* (9), 3762–3774.

(7) Dong, Z. Y.; Lewis, R. V.; Middaugh, C. R. *Arch. Biochem. Biophys.* **1991**, *284* (1), 53–57.

(8) Agnarsson, I.; Kuntner, M.; Blackledge, T. A. *PLoS One* **2010**, *5*, (9).

(9) Swanson, B. O.; Anderson, S. P.; DiGiovine, C.; Ross, R. N.; Dorsey, J. P. *Integr. Comp. Biol.* **2009**, *49* (1), 21–31.

(10) Swanson, B. O.; Blackledge, T. A.; Beltran, J.; Hayashi, C. Y. *Appl. Phys. A: Mater. Sci. Process.* **2006**, *82* (2), 213–218.

(11) Vollrath, F.; Knight, D. P. *Nature* **2001**, *410* (6828), 541–548.

(12) Gosline, J. M.; Denny, M. W.; Demont, M. E. *Nature* **1984**, *309* (5968), 551–552.

(13) Du, N.; Yang, Z.; Liu, X. Y.; Li, Y.; Xu, H. Y. *Adv. Funct. Mater.* **2011**, *21* (4), 772–778.

(14) Vollrath, F.; Porter, D. *Appl. Phys. A: Mater. Sci. Process.* **2006**, *82* (2), 205–212.

(15) Termonia, Y. *Macromolecules* **1994**, *27* (25), 7378–7381.

(16) Porter, D.; Vollrath, F. *Nano Today* **2007**, *2* (3), 6–6.
(17) Keten, S.; Buehler, M. J. *J. R. Soc., Interface* **2010**, *7* (53), 1709–1721.
(18) Keten, S.; Xu, Z. P.; Ihle, B.; Buehler, M. J. *Nat. Mater.* **2010**, *9* (4), 359–367.
(19) Nova, A.; Keten, S.; Pugno, N. M.; Redaelli, A.; Buehler, M. J. *Nano Lett.* **2010**, *10* (7), 2626–2634.
(20) Becker, N.; Oroudjev, E.; Mutz, S.; Cleveland, J. P.; Hansma, P. K.; Hayashi, C. Y.; Makarov, D. E.; Hansma, H. G. *Nat. Mater.* **2003**, *2* (4), 278–283.
(21) Zhou, H. J.; Zhang, Y. *Phys. Rev. Lett.* **2005**, *94*, (2).
(22) Papadopoulos, P.; Solter, J.; Kremer, F. *Colloid Polym. Sci.* **2009**, *287* (2), 231–236.
(23) Frische, S.; Maunsbach, A. B.; Vollrath, F. *J. Microsc. (Oxford, U. K.)* **1998**, *189*, 64–70.
(24) Thiel, B. L.; Viney, C. *J. Microsc. (Oxford, U. K.)* **1997**, *185*, 179–187.
(25) Poza, P.; Perez-Rigueiro, J.; Elices, M.; Llorca, J. *Eng. Fract. Mech.* **2002**, *69* (9), 1035–1048.
(26) Li, S. F. Y.; Mcghie, A. J.; Tang, S. L. *Biophys. J.* **1994**, *66* (4), 1209–1212.
(27) Vollrath, F.; Holtet, T.; Thogersen, H. C.; Frische, S. *Proc. R. Soc. London, Ser. B* **1996**, *263* (1367), 147–151.
(28) Du, N.; Liu, X. Y.; Narayanan, J.; Li, L. A.; Lim, M. L. M.; Li, D. Q. *Biophys. J.* **2006**, *91* (12), 4528–4535.
(29) Perez-Rigueiro, J.; Elices, M.; Plaza, G. R.; Rueda, J.; Guinea, G. V. *J. Polym. Sci., Part B: Polym. Phys.* **2007**, *45* (7), 786–793.
(30) Buehler, M. J.; Yung, Y. C. *Nat. Mater.* **2009**, *8* (3), 175–188.
(31) Denny, M. *J. Exp. Biol.* **1976**, *65* (2), 483–506.
(32) Augsten, K.; Muhlig, P.; Herrmann, C. *Scanning* **2000**, *22* (1), 12–15.
(33) Anderson, T. L. *Fracture mechanics: fundamentals and applications*. 3rd ed.; Taylor & Francis: Boca Raton, FL, 2005; p 621 p.
(34) Buehler, M. J.; Yao, H. M.; Gao, H. J.; Ji, B. H. *Modell. Simul. Mater. Sci. Eng.* **2006**, *14* (5), 799–816.
(35) Griffith, A. A. *Philos. Trans. R. Soc., A* **1920**, *221*, 163–198.
(36) Keten, S.; Buehler, M. J. *Nano Lett.* **2008**, *8* (2), 743–748.
(37) Keten, S.; Xu, Z.; Ihle, B.; Buehler, M. J. *Nat. Mater.* **2010**, *9* (4), 359–367.
(38) Ji, B. H. *J. Biomech.* **2008**, *41* (2), 259–266.
(39) Cranford, S. W.; Tarakanova, A.; Pugno, N.; Buehler, M. J. *In submission* 2011.
(40) Gao, H. J.; Ji, B. H.; Jager, I. L.; Arzt, E.; Fratzl, P. *Proc. Natl. Acad. Sci. U.S.A.* **2003**, *100* (10), 5597–5600.
(41) Gao, H. J.; Chen, S. H. *J. Appl. Mech. -Trans. ASME* **2005**, *72* (5), 732–737.
(42) Chou, T. W. *Microstructural design of fiber composites*. Cambridge University Press: 1992.
(43) Espinosa, H. D.; Rim, J. E.; Barthelat, F.; Buehler, M. J. *Prog. Mater. Sci.* **2009**, *54* (8), 1059–1100.
(44) Bosia, F.; Buehler, M. J.; Pugno, N. M. *Phys. Rev. E* **2010**, *82*, 5.
(45) Ji, B. H.; Gao, H. J. *J. Mech. Phys. Solids* **2004**, *52* (9), 1963–1990.
(46) Arslan, M.; Boyce, M. C. *J. Appl. Mech.* **2006**, *73* (4), 536–543.
(47) Tsai, D. H. *J. Chem. Phys.* **1979**, *70* (3), 1375–1382.
(48) Buehler, M. J.; Gao, H. J. *Nature* **2006**, *439* (7074), 307–310.
(49) Thiel, B. L.; Kunkel, D. D.; Viney, C. *Biopolymers* **1994**, *34* (8), 1089–1097.
(50) Plimpton, S. *J. Comput. Phys.* **1995**, *117* (1), 1–19.
(51) Tada, H.; Paris, P. C.; Irwin, G. R. *The stress analysis of cracks handbook*; 3rd ed.; ASME Press: New York, 2000; p 677.